Received: 31 May 2021 | Revised: 3 November 2021 | Accepted: 9 November 2021

DOI: 10.1002/joc.7447

International Journal of Climatology RMetS

RESEARCH ARTICLE

Evaluation of the seasonality and spatial aspects of the Southern Annular Mode in CMIP6 models

Xiaoqi Zhang[1,2] | Bian He[2,3] | Yimin Liu[2,3] | Qing Bao[2] | Fei Zheng[4,5] | Jinxiao Li[2] | Wenting Hu[2] | Guoxiong Wu[2,3]

[1]School of Atmospheric Sciences, Nanjing University of Information Science and Technology, Nanjing, China

[2]State Key Laboratory of Numerical Modeling for Atmospheric Sciences and Geophysical Fluid Dynamics (LASG), Institute of Atmospheric Physics, Chinese Academy of Sciences, Beijing, China

[3]College of Earth and Planetary Sciences, University of Chinese Academy of Sciences, Beijing, China

[4]School of Atmospheric Sciences, Key Laboratory of Tropical Atmosphere-Ocean System, Ministry of Education, Sun Yat-sen University, Zhuhai, China

[5]Southern Marine Science and Engineering Guangdong Laboratory, Zhuhai, China

Correspondence
Bian He and Yimin Liu, State Key Laboratory of Numerical Modeling for Atmospheric Sciences and Geophysical Fluid, Dynamics (LASG), Institute of Atmospheric Physics, Chinese Academy of Sciences, Beijing 100029, China.
Email: heb@lasg.iap.ac.cn (B. H.) and lym@lasg.iap.ac.cn (Y. L.)

Funding information
Strategic Priority Research Program of the Chinese Academy of Sciences, Grant/Award Number: XDA19070404; National Key Research and Development Program of China, Grant/Award Numbers: 2020YFA0608903, 2017YFA0604004; National Natural Science Foundation of China, Grant/Award Number: 42030602

Abstract

The simulation skills of the Southern Annular Mode (SAM) pattern for the CMIP6 models are evaluated in this study. Both the Atmospheric Model Intercomparison Project (AMIP) and historical experiments are utilized to understand the effect of SST forcing and air–sea interaction. The spatial correlation coefficient, standard deviation, and root-mean-square error (RMSE) are used as the objective metrics. The results suggest that the multimodel mean (MME) for both AMIP and historical data could capture the basic spatial patterns of the SAM for all seasons, featuring the opposite sign between the middle and high latitudes with a zonal three-wave structure in the middle latitudes (positive phase). However, the overall skill of the AMIP simulation is higher than that of the historical simulation, which could be attributed to realistic SST forcing being applied. The simulation skill varies for different seasons: the skill for boreal spring (March–May [MAM]) is the lowest, while it is highest in boreal winter (December–February [DJF]). Further analysis shows that the simulations of the SAM asymmetric part are the key component for the simulation of the spatial pattern of the SAM, especially sensitive in MAM. The wave–current interaction simulation at mid–high latitudes is suggested to be improved for the advancement of SAM simulations in future model development.

KEYWORDS

AMIP, CMIP6, historical, model evaluation, seasonal variation, Southern Annular Mode

1 | INTRODUCTION

The Southern Hemisphere annular mode (SAM) is the primary mode of extratropical circulation variability in the Southern Hemisphere (Gong and Wang 1998, 1999; Thompson and Wallace, 2000; Thompson *et al*., 2000). The SAM is also referred to as the Antarctic Oscillation (AAO), which is characterized by a pressure or geopotential height anomaly in the zonal symmetric dipole mode between high latitudes and midlatitudes from sea level to the stratosphere, which is mainly related to wave–current interactions (Limpasuvan and Hartmann, 1999).

Previous studies have revealed that the SAM is important for weather and climate change in the Southern Hemisphere (SH). For example, the SAM is related to changes in Antarctic sea ice and daily precipitation anomalies in Australia (Lefebvre *et al*., 2004; Hendon *et al*., 2007). The SAM is related to anomalies in some regions, such as cold anomalies in parts of Antarctica, and anomalously dry conditions and more settled weather in New Zealand (Kwok and Comiso, 2002; Thompson and Solomon, 2002). The SAM is closely related to polar jet; a strengthening and poleward shifting of the polar jet occur during the positive SAM (Kidson and Sinclair, 1995). Below the surface through the mixed layer, a general warming of the Southern Ocean has also been suggested to be linked to the changes in the SAM (Gille, 2008; Spence *et al*., 2014; Ferreira *et al*., 2015).

The SAM is also related to the climate in the Northern Hemisphere, such as summer rainfall in the middle and lower reaches of the Yangtze River, winter precipitation over southern China, Indian summer monsoon precipitation, and positive tripole precipitation patterns (two positive anomalies cover the equator and midlatitude regions, with one negative anomalies over the subtropics) in the Northern Hemisphere (Nan *et al*., 2003; Wu *et al*., 2015; Zheng *et al*., 2015; Dou *et al*., 2017; Liu *et al*., 2018). In addition, the SAM also has important implications for the prediction of the Northern Hemisphere monsoon (Nan *et al*., 2009; Wu *et al*., 2009; Liu *et al*., 2018). Therefore, the simulation of the SAM is crucial for climate prediction.

Studies in recent years have shown that the SAM trend is positive in the observation data, which is reproduced in most models. The IPCC AR4 models capture the recent (1957–2005) positive SAM trends in austral summer, and ozone depletion is the dominant mechanism driving these trends (Fogt *et al*., 2009). Gillett and Fyfe (2013) investigated the simulated changes in the annular modes in the historical and RCP4.5 scenario simulations of 37 models from the CMIP5 generation. The CMIP5 models simulate a significant negative SAM response to volcanic aerosols in boreal spring (March–May [MAM]) and boreal summer (July–August [JJA]) and a significant positive SAM response to solar irradiance variations in MAM, JJA, and boreal winter (December–February [DJF]) (Gillett and Fyfe, 2013). The DJF SAM index shows a strong upward trend to 2000 and then remains approximately constant through the 21st century, likely due to the counteracting influence of greenhouse gas increases and ozone recovery (Gillett and Fyfe, 2013). Morgenstern (Morgenstern, 2021) evaluated the SAM trends in CMIP6 simulations. A strengthening of the SAM in DJF is attributed nearly completely to ozone depletion because a further strengthening influence due to longlived greenhouse gases is almost fully counterbalanced by a weakening influence due to stratospheric ozone increases associated with these greenhouse gas increases (Morgenstern, 2021).

Previous studies have examined the performances of the models in simulating the spatial pattern of the SAM. Zheng *et al*. (2013) documented that the CMIP5 models could basically reproduce the spatial pattern of the SAM in DJF. Three models (MIROC-ESM-CHEM, FGOALS-s2, and BCC_CSM1.1) overestimated the amplitude of the SAM pattern, while the other models underestimated the amplitude of the SAM pattern (Zheng *et al*., 2013). The ability of CAMS-CSM to simulate the horizontal and vertical structures of the SAM is good in four seasons, but CAMS-CSM exaggerates the amplitude of the SAM in all four seasons (Nan *et al*., 2019). Lee *et al*. (2019) found that the SAM patterns of the E3SM simulations in austral spring and summer (SON and DJF) were in better agreement with the observations than those in austral autumn and winter (MAM and JJA).

The sixth phase of the Coupled Model Intercomparison Project (CMIP6) provides climate simulations from state-of-the-art climate models. The overall simulation skill on SAM remains unknown. Furthermore, previous studies mainly focused on understanding the trend or the SAM index but focused less on the spatial patterns of the SAM in different seasons. And most research focused on the symmetrical part of SAM, such as the definition of the SAM index (Baldwin and Thompson, 2009; Ho *et al*., 2012). However, some studies have explored the relationship between the asymmetric part of the SAM and the dynamic process or SST (Codron, 2007; Kidston *et al*., 2009; Ding *et al*., 2012). Few studies have evaluated the asymmetric part of the SAM or explored the relationship between the asymmetric part of the SAM and the SAM spatial patterns. Since the SAM pattern has a close relationship with the local weather and climate change in the SH, the evaluation of the SAM pattern simulation is important for the understanding and improvement of climate models. In the design of CMIP6, both Atmospheric Model Intercomparison Project (AMIP) and historical experiments are important to understand the

simulation ability and model bias for climate simulation. Therefore, in this study, we will to evaluate the simulation of SAM in both the AMIP experiments and historical experiments of CMIP6 to understand the performance of the state-of-the-art CMIP6 climate models in capturing the seasonal distributions of the SAM simulation and the differences between the AMIP and historical simulations. These evaluations will benefit the understanding of SAM simulation and model development.

The manuscript is organized as follows: In section 2, the reference data, CMIP6 experiments and the associated models, and the objective metrics employed in our study are all presented. In section 3.1, the seasonal variation in the SAM spatial patterns in ERA-Interim are presented. In section 3.2, the simulation skills of the SAM spatial patterns for four seasons are quantitatively evaluated for the CMIP6 multimodels. In section 3.3, simulations of the asymmetric part of the SAM are evaluated, and the possible causes of simulation bias are discussed. Finally, the discussion and conclusions are presented in section 4.

2 | DATASETS, MODELS, AND METHODS

2.1 | Reanalysis data

The reference data used in this study are the ERA-Interim data, which are produced by the European Centre for Medium Range Weather Forecasts (ECWMF) to replace ERA-40. ERA-Interim is a global atmospheric reanalysis that is available from January 1, 1979 to August 31, 2019 (Dee *et al*., 2011). The ERA-Interim monthly data have a resolution of $1.5^\circ \times 1.5^\circ$. The data can be downloaded from https://www.ecmwf.int/en/forecasts/datasets/reanalysis-datasets/era-interim.

2.2 | Model data

The CMIP6 AMIP and historical experiments are used in this study. AMIP (Gates *et al*., 1999) simulations are useful for evaluating the skill of the atmospheric model component. The simulations are constrained by the observed sea surface temperature (SST) and sea ice concentration. The historical simulations in the CMIP6 (Eyring *et al*., 2016) can be used to better understand climate change arising from natural forcing, anthropogenic forcing, and unforced variability. These simulations over the period of 1850–2014 are forced by externally imposed conditions, such as solar variability, volcanic aerosols, and human-induced changes (greenhouse gases and anthropogenic aerosols) based on observations. AMIP experiments and historical simulations are well suited for quantifying and understanding important climate change response characteristics.

There are 15 models selected from both the AMIP and historical experiments, as listed in Table 1. The model's name in the historical experiment is consistent with the AMIP experiment. In this study, there are 67 ensemble members available in the AMIP experiment and 175 ensemble members available in the historical experiment. See Table 1 for details of the two experiments. To facilitate the comparison of AMIP experiments and historical experiments, we used the period of 1979–2014 for both experiments. The resolutions of all data are interpolated to the resolutions of the ERA-Interim data. The model datasets can be downloaded from https://esgf-node.llnl.gov/projects/cmip6/.

2.3 | Methods

The SAM pattern is obtained by the leading empirical orthogonal function (EOF) mode of the sea level pressure (PSL) southward of 20°S and then the PSL regression of its PC1 time series (Mo, 2000; Zheng *et al*., 2013; Nan *et al*., 2019). The seasonally averaged SAM spatial pattern is obtained from the monthly data. The four seasons are DJF (boreal winter or austral summer), MAM (boreal spring or austral autumn), JJA (boreal summer or austral winter), and September–November (SON; boreal autumn or austral spring).

Taylor diagrams are especially useful in evaluating multiple aspects of complex models or in gauging the relative skills of many different models (Taylor, 2001; 2005). The spatial correlation coefficient and the standard deviation ratio are used as two important statistics in the Taylor diagram. The spatial correlation coefficient can characterize the similarity between the test field and the reference field. The standard deviation ratio is the standard deviation of the spatial pattern of the model SAM to the standard deviation of the SAM pattern in ERA-Interim. The standard deviation ratio can therefore characterize the amplitude intensity of the test field relative to the reference field.

To quantify the bias of the simulation, we define an index for the measurement as the root-mean-square error (RMSE). The formula is described as follows:

$$\mathrm{RMSE} = \sqrt{(1-\mathrm{cor})^2 + (1-\mathrm{ratio})^2}, \quad (1)$$

where cor is the spatial correlation coefficient between the models and reanalysis data, and the ratio is the standard deviation ratio. Spatial correlation coefficients and

TABLE 1 List of CMIP6 models used in this study

Model name	Model centre	Ensemble size	References
BCC-CSM2-MR	Beijing Climate Center, China	3 (3)	Wu *et al.* (2019)
BCC-ESM1	Beijing Climate Center, China	3 (3)	Wu *et al.* (2020)
CESM2-WACCM	NCAR, USA	3 (3)	Gettelman (2019)
CESM2	NCAR, USA	1 (9)	Danabasoglu (2020)
CNRM-CM6-1	CNRM, CERFACS, France	1 (10)	Voldoire *et al.* (2019)
CNRM-ESM2-1	CNRM, CERFACS, France	1 (5)	Séférian *et al.* (2019)
FGOALS-f3-L	IAP, China	6 (3)	He *et al.* (2019)
MIROC6	JAMSTEC AORI, NIES, and R-CCS, Japan	10 (10)	Tatebe *et al.* (2019)
MRI-ESM2-0	Meteorological Research Institute, Japan	3 (6)	Yukimoto *et al.* (2019)
GFDL-CM4	National Oceanic and Atmospheric Administration, Geophysical Fluid Dynamics Laboratory, Princeton, USA	1 (1)	Dunne *et al.* (2020)
GISS-E2-1-G	Goddard Institute for Space Studies, USA	15 (27)	Ito *et al.* (2020)
IPSL-CM6A-LR	Institut Pierre Simon Laplace, Paris, France	11 (31)	Boucher *et al.* (2020)
SAM0-UNICON	Seoul National University, Republic of Korea	1 (1)	Park *et al.* (2019)
UKESM1-0-LL	Met Office Hadley Centre, Fitzroy Road, Exeter, UK	1 (13)	Sellar *et al.* (2019)
CanESM5	Canadian Centre for Climate Modelling and Analysis, Environment And Climate Change Canada, Canada	7 (50)	Swart *et al.* (2019)

Note: The number in parentheses represents the number of ensembles in the historical experiment. The numbers outside the brackets represent the number of ensembles in the AMIP experiment.

standard deviation ratios are two important parameters for the simulation model evaluation of Taylor plots (Taylor, 2001).

The asymmetric part of the SAM is defined as follows:

$$P'_* = P - P' - P_*, \tag{2}$$

where P represents PSL, P' presents its time mean, and P_* presents its zonal mean (Fogt *et al.*, 2012). P'_* is the PSL with the time average and zonal mean removed. Then, P'_* is used to regress the PC1 time series of the PSL to obtain the asymmetric part of the SAM.

3 | RESULTS

3.1 | Observed SAM pattern

The observed SAM spatial patterns for all seasons during 1979–2014 are shown in Figure 1a–d. The leading modes (EOF1) account for 34.3–41.1% of the total variance for the four seasons in the ERA-Interim reanalysis. The variance of DJF is the highest, and that of JJA is the lowest. These SAM patterns are also very close to the results in the NCEP1, JRA55, and ERA5 reanalysis datasets and these patterns is quite robust, as shown in Figures S1, S3, S5, and S6, Supporting Information. On the other hand, many studies have used ERA-Interim reanalysis as the reference dataset for the analysis of the SAM (Yali and Huijun, 2010; Qian *et al.*, 2011; Nan *et al.*, 2019). Therefore, in this study, the ERA-Interim datasets are chosen as the reference datasets for the evaluations.

The positive SAM phases in the four seasons are generally similar, with the high latitudes and midlatitudes having the opposite phase. The Antarctic continent is a low-pressure area, and midlatitudes are a high-pressure area with a zonal three-wave structure. However, compared with the other three seasons, the SAM amplitude is weaker, and the spatial pattern of the SAM is more zonally symmetrical in DJF (Figure 1a). This result is consistent with the conclusion of Kidston *et al.* (2009). The negative centres all expand to the South Pacific region in MAM (Figure 1b), JJA (Figure 1c), and SON (Figure 1d), while two positive centres are especially intensified over the south Indian Ocean and south Pacific Ocean in these seasons. The positive centre over the South Atlantic Ocean is strongest in MAM and weaker in JJA and SON. The observed SAM patterns for all the seasons calculated in this study are consistent with those of previous studies (Lu *et al.*, 2007; Nan *et al.*, 2019).

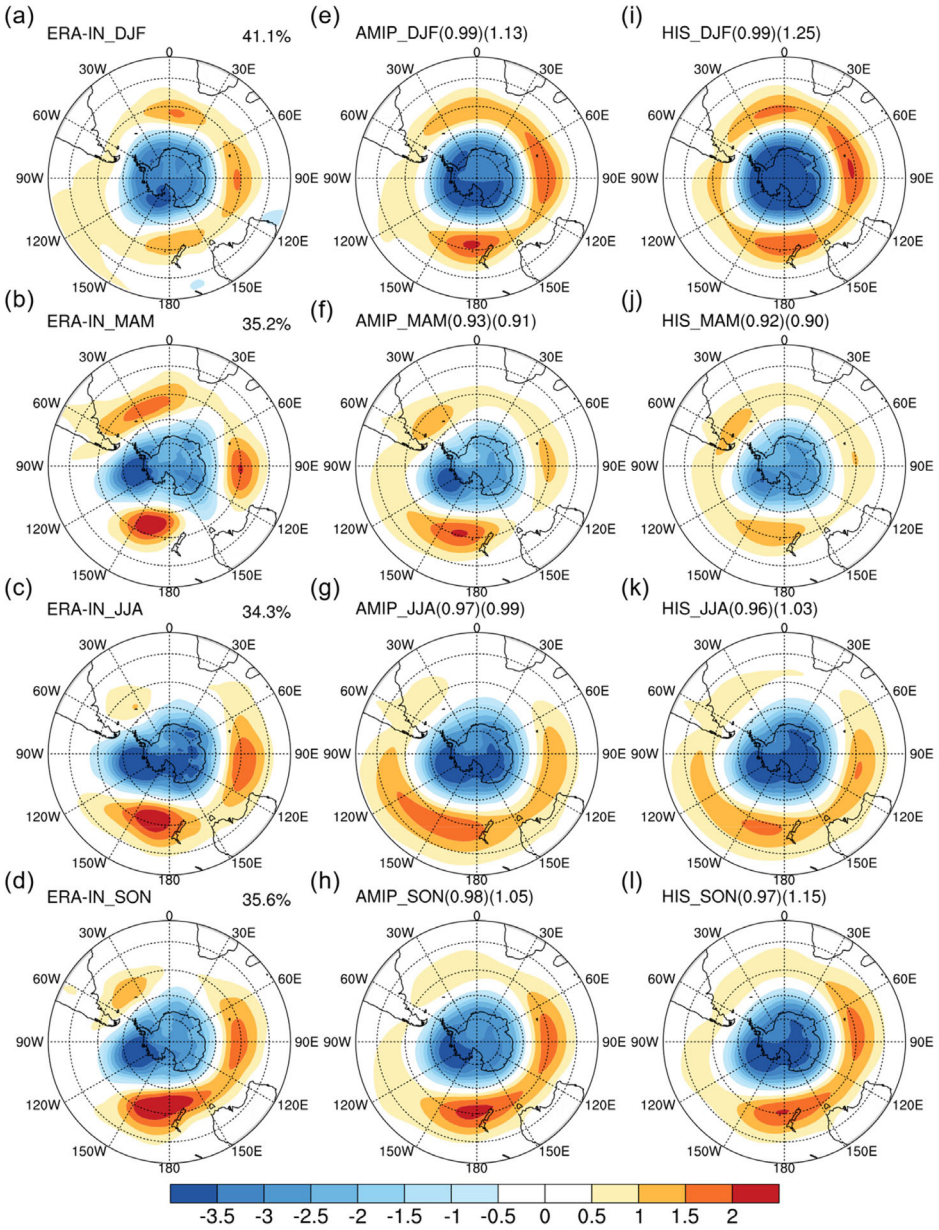

FIGURE 1 Spatial pattern of the SAM as the leading EOF mode at the PSL south of 20°S for the four seasons in ERA-Interim and the multimodel ensemble mean (MME). From left to right (e–l), the number in the first bracket indicates the correlation coefficient, and the number in the second bracket indicates the standard deviation ratio [Colour figure can be viewed at wileyonlinelibrary.com]

3.2 | Evaluation of the SAM pattern for both AMIP and historical simulations

AMIP and historical simulations are both important standard experiments for model evaluation. The AMIP simulation applied observed SST and SIC forcing, which overcome the SST bias simulated in the air–sea coupled simulation, while the historical run could especially investigate the air–sea coupled processes in the climate simulation. In this study, 15 models are used for both the AMIP experiment and the historical experiment (Table 1). The multimodel ensemble mean (MME) is commonly proposed as an effective way to reduce the individual model noise in climate simulations. We show the seasonal SAM pattern of MME for both AMIP (Figure 1e–h) and historical (Figure 1i–l) simulations in Figure 1. Overall, the SAM pattern is well captured in both AMIP and historical experiments. The correlation coefficient is the highest in DJF. However, the amplitudes of both experiments are stronger than ERA-Interim in DJF (1.13 for AMIP and 1.25 for historical) and weaker in MAM (0.91 for AMIP and 0.90 for historical). In JJA, the positive anomaly centres in the south Pacific Ocean in both AMIP and historical data are underestimated. In SON, the positive centre near South America is underestimated in both experiments. Finally, based on the correlation and standardized deviation, the simulation skill of AMIP is overall slightly higher than the historical skill, which implies that the observed SST forcing partly favours the good simulation of the SAM pattern.

The quantitative understanding of the individual model skill in capturing the SAM pattern is analysed by the Taylor diagram in Figure 2. It is clear that the group

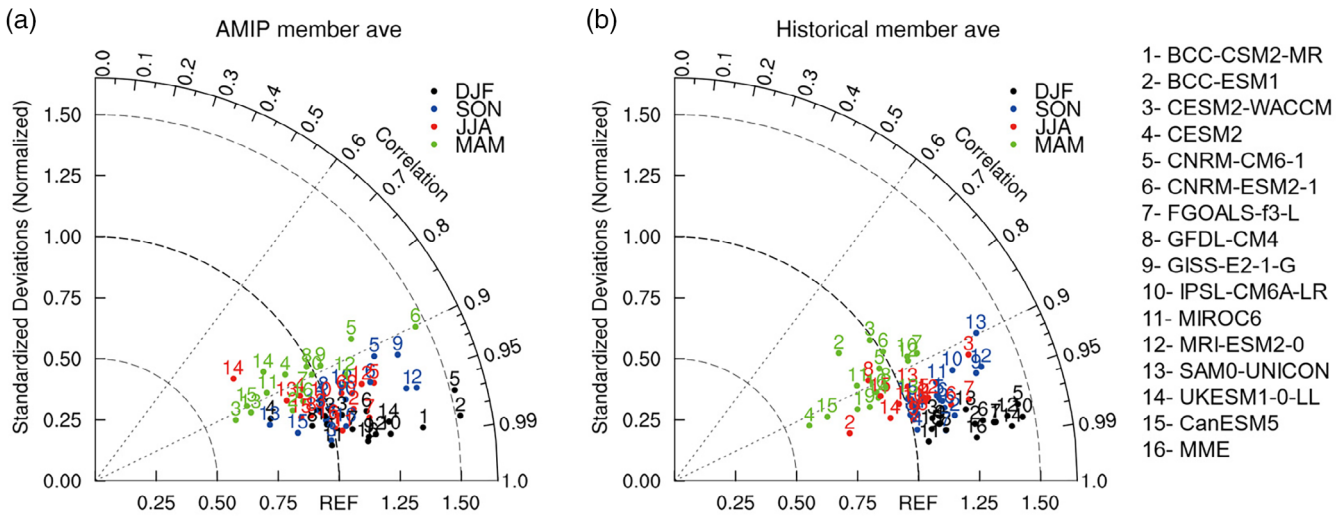

FIGURE 2 Taylor diagram of the SAM pattern simulation (with ERA-Interim), which is the single-model ensemble mean of the ensemble members (SME) and MME in the (a) AMIP experiment and (b) the historical experiment [Colour figure can be viewed at wileyonlinelibrary.com]

of DJF simulations is overall better than the other seasons according to the correlation coefficients in both AMIP and historical experiments, while the skill of MAM is the lowest for almost all the models. For the AMIP simulation, some models simulate a stronger amplitude of SAM (close to 1.5), such as BCC-ESM1 and CNRM-CM6-1 for the DJF season and CNRM-ESM2-1 for MAM, and some models underestimate nearly half of the amplitude, such as CESM2-WACCM for MAM. For the historical simulation, IPSL-CM6A-LR simulates the strongest SAM in DJF, while CESM2 simulates the weakest SAM in MAM. Moreover, MIROC6 simulates both the best scores of correlation and standardized deviations in AMIP and historical experiments. Except for these individual model simulation results, a large number of models simulate stronger amplitudes in DJF for both the AMIP and historical experiments while additionally underestimating the SAM amplitude in MAM for the historical experiments.

Ensemble simulations are conventional methods to reduce individual model noise in climate simulations. Therefore, the number of model members may also be important in simulating SAM for state-of-the-art models to investigate the sensitivity of SAM simulations from the model member quantity. We show the box plots for the spatial correlation coefficient and standard deviation ratio of each model in Figures 3 and 4, respectively. One box is composed of the median, maximum, minimum, upper quartile, and lower quartile. Hereinafter, these five values are collectively referred to as five characteristic values. When the number of model ensemble members is less than 5, dots are plotted instead of the boxes. In Figures 3 and 4, the AMIP and historical experiments are shown in red and blue, respectively. The brackets after each model name denote the number of ensemble members.

For the pattern simulation, the box plots in Figure 3 show that the correlation is above 0.9 for almost all the experiments in both AMIP and historical DJF (Figure 3a), while the correlation spreads to a large range from 0 to 0.97 in MAM (Figure 3b), especially for the historical experiments. In JJA (Figure 3c), the model spread ranges from 0.5 to 0.97, and the large spread mainly occurs among the historical experiments, such as CESM2, GISS-E2-1-G, IPSL-CM6A-LR, MIROC6, and CanESM5. In SON (Figure 3d), the model spread mainly ranges from 0.65 to 0.97, while the large spread models are FGOALS-f3-L, IPSL-CM6A-LR, MIROC6, and CanESM5. The above results suggest that the model spread in the simulated SAM pattern is seasonally dependent. The simulations are less sensitive to the model member quantity in DJF but quite sensitive in other seasons, especially in MAM for both AMIP and historical experiments. Therefore, MAM, JJA and SON, the SAM pattern is sensitive to the number of ensemble members suggesting that sampling variability has an impact on the calculation of the SAM pattern.

The uncertainty of the SAM pattern simulation from the initial perturbation of an individual model can be deduced by the length of the box, which depends on the distance among the five characteristic values. For example, CESM2 is very sensitive to the initial condition for capturing the SAM pattern during MAM in the historical simulation (Figure 3b) since the box ranges from nearly zero to 0.95 based on a total of 9 ensemble members. However, for GISS-E2-1-G and IPSL-CM6A-LR, the box

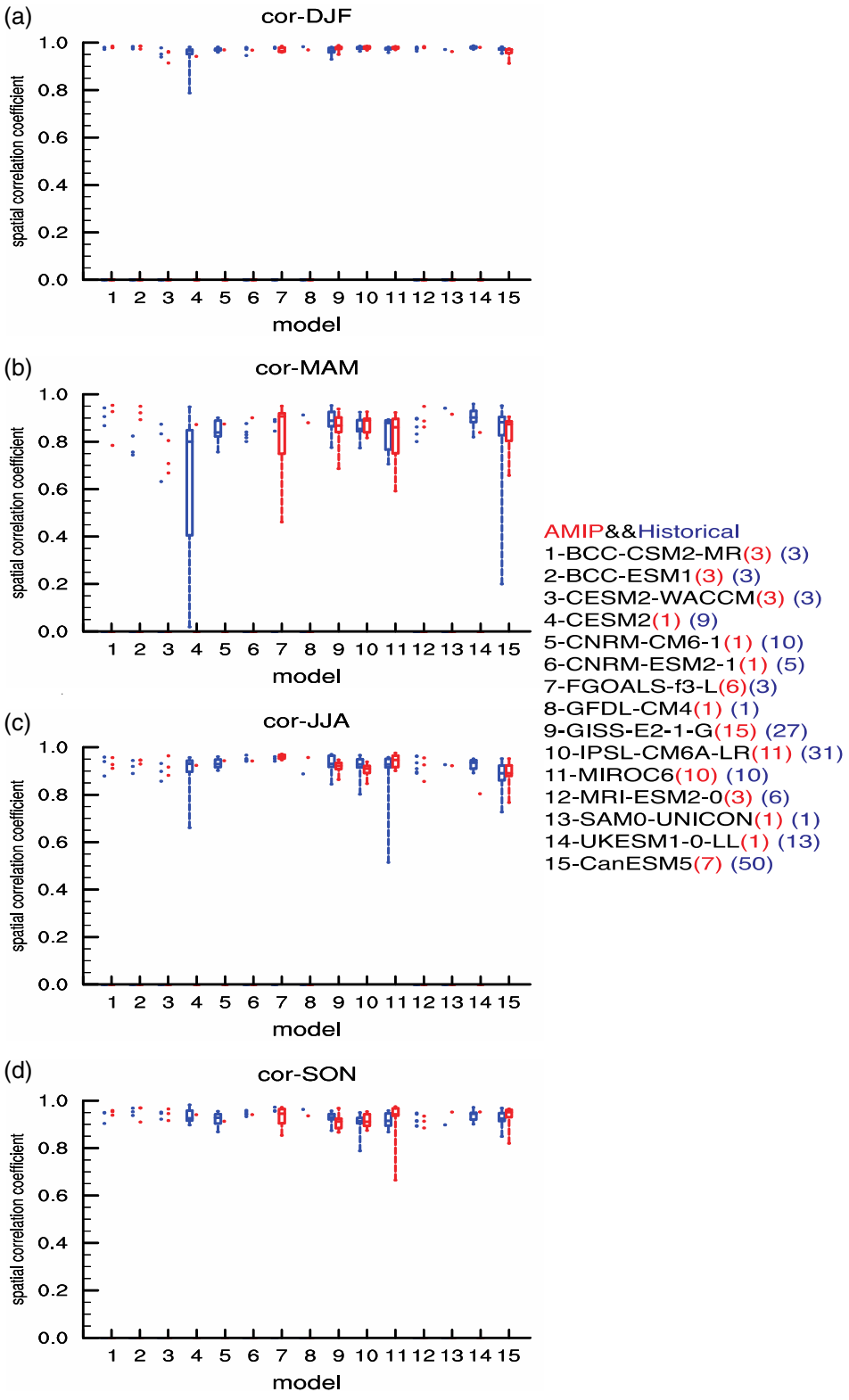

FIGURE 3 Correlation coefficients (with ERA-Interim) of the SAM pattern simulation from individual ensembles in the AMIP and the historical experiments for the four seasons. The *X*-axis represents all models, and the *Y*-axis represents the spatial correlation coefficient. The red number indicates the number of ensembles in the model for the AMIP experiment, and the blue number indicates the number of ensembles in the model for the historical experiment [Colour figure can be viewed at wileyonlinelibrary.com]

length is quite short relative to other models during MAM, JJA, and SON for both AMIP and historical experiments. This means that the simulation skills of these two models are less sensitive to the initial perturbation than the inherent physics of the model. The above analysis suggests that the large ensemble simulation is favoured for the individual model to reduce the signal-to-noise ratio for the SAM pattern simulation, especially in the MAM season. However, the simulation skill not only relies on the ensemble numbers but is also more related

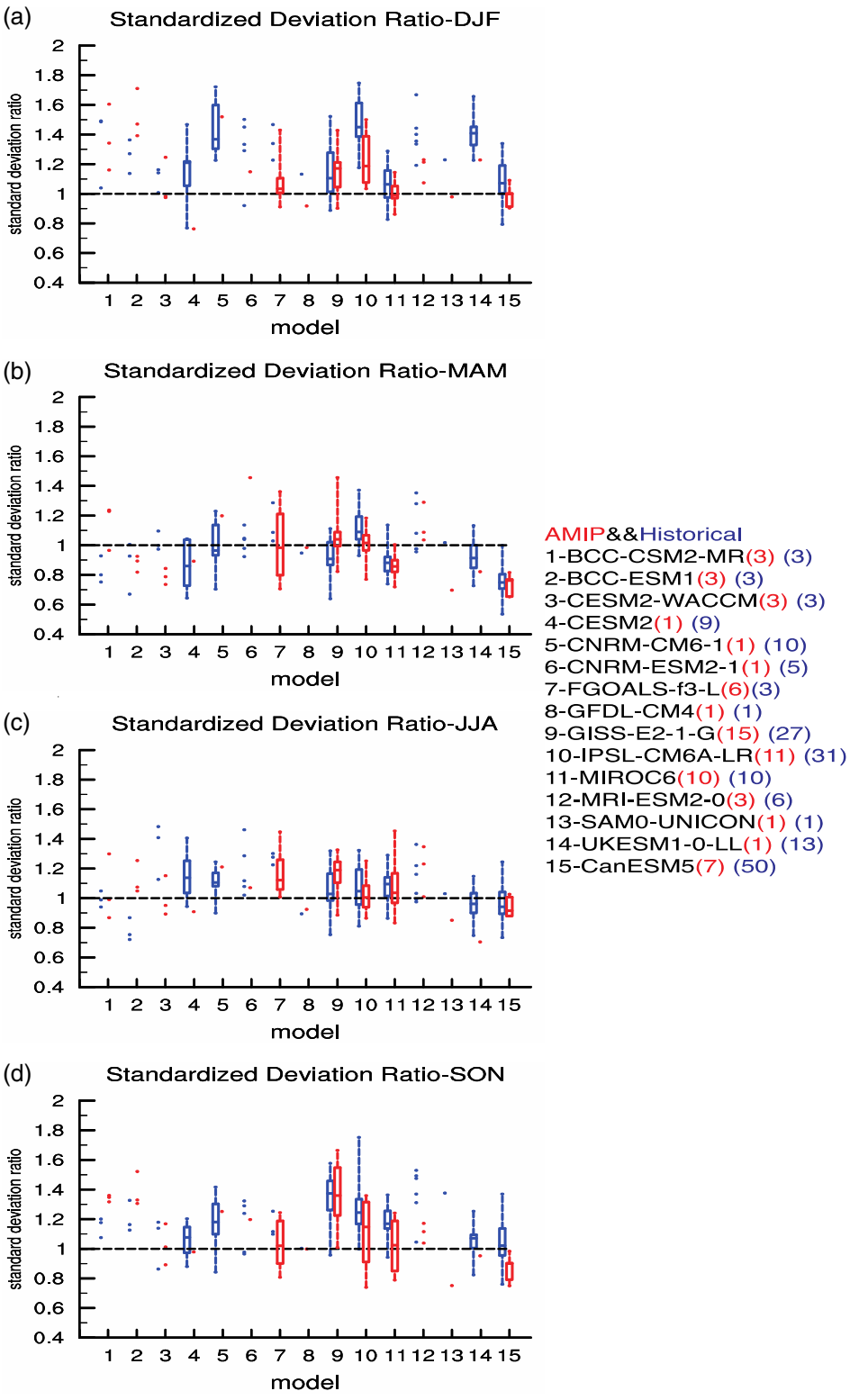

FIGURE 4 Standard deviation ratio (with ERA-Interim) of the SAM simulation from the individual ensembles in the AMIP and the historical experiments for the four seasons. The *X*-axis represents all models, and the *Y*-axis represents the standard deviation ratio. The red number indicates the number of ensembles in the model for the AMIP experiment, and the blue number indicates the number of ensembles in the model for the historical experiment [Colour figure can be viewed at wileyonlinelibrary.com]

to the model physics parameterization, which influences the atmospheric dynamics simulation.

The AMIP simulations are constrained by the observed SST and sea ice concentration, while the historical experiment is an air–sea coupled simulation. The AMIP simulation overcomes the influence of the SST bias on the SAM simulation. We would like to know if the SAM pattern simulation skill is substantially different between these two kinds of experiments. Since the simulation skills are both very high in DJF, we only evaluated the AMIP and historical simulations during MAM, JJA, and SON. There are four models that provide appreciable

numbers of ensemble members, such as GISS-E2-1-G, IPSL-CM6A-LR, MIROC6, and CanESM5. In MAM (Figure 3b), the historical simulation skill is higher than AMIP for GISS-E2-1-G and CanESM5 but comparable with AMIP for IPSL-CM6A-LR and MIROC6. In JJA (Figure 3c), the historical simulation skill is higher than AMIP for GISS-E2-1-G and IPSL-CM6A-LR, while the AMIP simulation skill is higher than historical for MIROC6 and is compatible with historical for CanESM5. In SON (Figure 3d), the historical simulation skill is higher than AMIP only for GISS-E2-1-G and lower than AMIP for the other three models. Overall, the AMIP simulation skill in capturing the SAM pattern is comparable to that of historical simulations, which suggests that the SST or air–sea coupling plays a secondary role in the SAM pattern simulation.

The influence of the initial perturbation on the amplitude strength of the SAM simulation is investigated in Figure 4, which shows the standardized deviation ratio for the multimodels. When the standard deviation ratio is closer to 1, the amplitude of the SAM simulation is closer to the ERA-Interim. It is clear that the seasonal variation of the amplitude simulation is not sensitive to the member quantity, which differs much from the pattern correlation. In general, the amplitudes of the SAM simulation in most models are overestimated in DJF (Figure 4a), JJA (Figure 4c), and SON (Figure 4d) but underestimated in MAM (Figure 4b) for both the AMIP experiment and the historical experiments. Meanwhile, for the comparison between AMIP and historical simulation, there are three models (IPSL-CM6A-LR, MIROC6, and CanESM5) which provided enough ensemble members for both AMIP and historical runs, shows larger amplitude in historical than AMIP for DJF, MAM and SON, while comparable in JJA. However, for GISS-E2-1-G, the AMIP simulation's amplitude is larger than historical simulations in MAM, JJA, and SON.

The above analysis shows that the ensemble members can partly or dominantly influence the total SAM simulation skill for individual models. Regarding the seasonal differences of the model skill, we would like to determine if it still exists or how much it is affected when the bias from the initial perturbation is excluded to understand the state-of-the-art model's best capability in capturing the SAM pattern simulation. The best simulation for each model is selected based on the RMSE, as shown in formula (1). When the correlation coefficient and standard deviation ratio are close to 1 (RMSE close to 0), the simulation result will be the closest to that of ERA-Interim. Therefore, the ensemble member with the minimal RMSE (and RMSE <0.1) is selected (Table 2). It is worth noting that models with only one ensemble member are removed.

TABLE 2 Selected model ensembles with the best simulations

Model	AMIP	Historical
BCC-CSM2-MR	JJA: r1i1p1f1	DJF: r3i1p1f1 JJA: r1i1p1f1 SON: r3i1p1f1
BCC-ESM1	JJA: r2i1p1f1	
CESM2-WACCM	DJF: r1i1p1f1 JJA: r1i1p1f1 SON: r1i1p1f1	DJF: r3i1p1f1
CESM2		DJF: r10i1p1f1 JJA: r7i1p1f1 SON: r5i1p1f1
CNRM-CM6-1		JJA: r3i1p1f2
CNRM-ESM2-1		DJF: r3i1p1f2 JJA: r5i1p1f2 SON: r1i1p1f2
FGOALS-f3-L	DJF: r5i1p1f1 JJA: r2i1p1f1 SON: r1i1p1f1	
MIROC6	DJF: r5i1p1f1 JJA: r6i1p1f1 SON: r2i1p1f1	DJF: r2i1p1f1 JJA: r8i1p1f1 SON: r3i1p1f1
MRI-ESM2-0	DJF: r3i1p1f1 JJA: r2i1p1f1 SON: r3i1p1f1	JJA: r1i2p1f1 SON: r4i1p1f1
GISS-E2-1-G	DJF: r3i1p3f1 MAM: r3i1p5f1 JJA: r2i1p5f1 SON: r4i1p1f1	DJF: r8i1p1f2 MAM: r8i1p1f1 JJA: r6i1p1f1 SON: r8i1p1f1
IPSL-CM6A-LR	DJF: r7i1p1f1 JJA: r6i1p1f1 SON: r10i1p1f1	JJA: r26i1p1f1 SON: r12i1p1f1
UKESM1-0-LL		MAM: r8i1p1f2 JJA: r9i1p1f2 SON: r4i1p1f2
CanESM5	DJF: r1i1p1f1 JJA: r3i1p2f1 SON: r1i1p1f1	DJF: r21i1p1f1 JJA: r12i1p1f1 SON: r17i1p1f1

Figure 5 shows the Taylor diagrams of all model ensemble members (with minimal RMSE). For the AMIP simulation (Figure 5a), the correlation coefficients in DJF and SON are generally better than those in MAM and JJA. In DJF, the standard deviation ratio of most models is greater than 1; that is, the SAM amplitude simulation is relatively strong. This result is quite similar to the MME shown in Figure 2a, which implies that the seasonal differences in the simulation skill cannot be reduced by increasing ensemble members. The evaluation of historical experiments (Figure 5b) is also quite similar to AMIP: the skill in DJF is the best, while the MAM is the lowest. However, compared to the MME

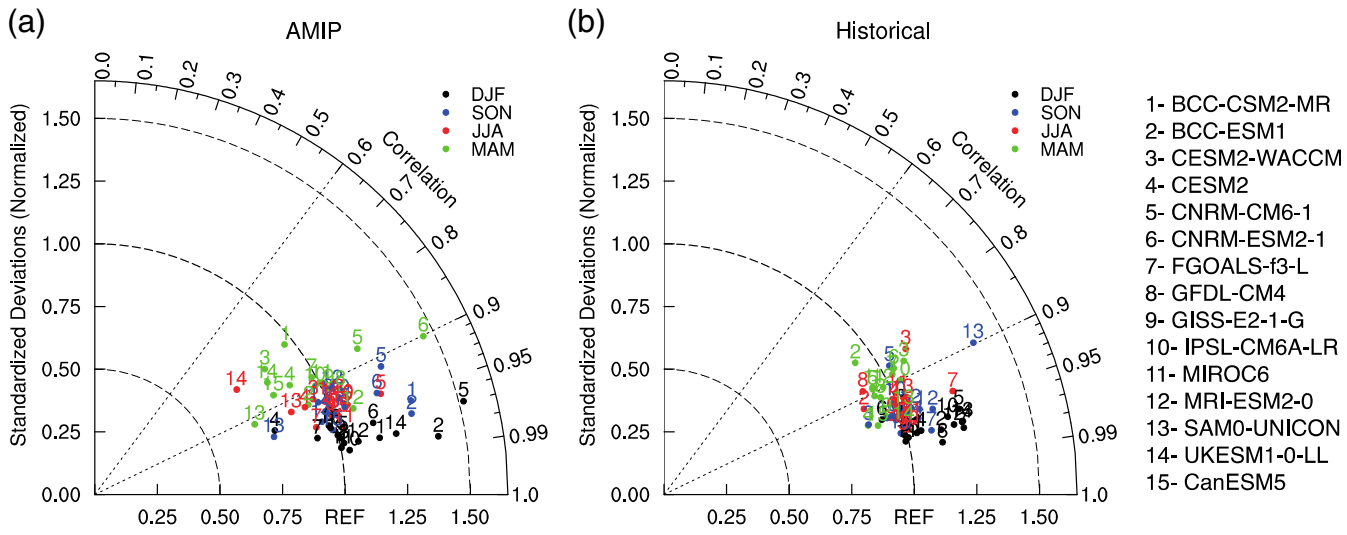

FIGURE 5 Taylor diagram of the SAM pattern simulation (with ERA-Interim), in which the minimum RMSE of the individual model in the (a) AMIP experiment and the (b) historical experiment are the lowest [Colour figure can be viewed at wileyonlinelibrary.com]

results (Figure 2b), the standard deviation is smaller in Figure 5b. This result indicates that the SAM amplitude simulation is sensitive to ensemble members when air–sea interaction is involved.

The spatial patterns for the ensemble mean of the best model members (Table 2) are shown in Figure 6. Overall, these patterns are similar to the ensemble mean composed of all the ensemble members in Figure 1. However, there are still some differences. For example, the amplitude simulation in the historical experiment is weaker and improved in DJF (Figure 6i), which is closer to the ERA-Interim. In MAM, the amplitude simulation in both AMIP (Figure 6f) and historical data (Figure 6j) is stronger and improved. Furthermore, in DJF (Figure 6e,i), neither the AMIP experiment nor the historical experiment seemed to simulate the positive centre of the South Atlantic well. The positive centre of the South Atlantic is overestimated in MAM for the AMIP simulations (Figure 6f). For JJA and SON, the positive centres in the South Pacific and South Atlantic are weak in both experiments (Figure 6g,k,h,l).

3.3 | Simulations of the SAM asymmetric component

It is important to note that the annular mode is a result of the wave–mean flow interaction and that the asymmetric part of the SAM is a key component in the total SAM (Zhao *et al.*, 2012; Nan *et al.*, 2019). The SAM symmetry part for the MME has also been calculated. It shows that the patterns are quite similar as that in ERA-Interim (Figure S2 in OSM). The simulation of the SAM asymmetric part could influence the total field of the SAM. To investigate how much the simulation of the asymmetric part affects the simulation of the SAM, the correlation coefficient and standard deviation ratio of the asymmetric part are evaluated in this subsection. Figure 7 shows the asymmetric part of the SAM in the reanalysis data and MME for the four seasons. Basically, there is a three-wave structure in the mid-high latitudes for all four seasons. By using the data of different decades for comparison, the asymmetric part of the SAM in the reanalysis is quite robust in most of the seasons (Figure S4 in OSM). The observed asymmetric part of the SAM is weakest in DJF (Figure 7a), and the asymmetric part is strongest in MAM (Figure 7b). In DJF (Figure 7a), there is a weak positive centre in the South Atlantic, South Pacific, and South Indian Oceans and a weak negative centre in the South Pacific. In MAM (Figure 7b), there is a robust positive centre and a robust negative centre in three major ocean basins surrounding Antarctica. The SAM pattern in JJA is similar to the pattern in SON, with a positive centre in three major ocean basins surrounding Antarctica and a negative centre in the South Pacific (Figure 7c,d).

The correlation coefficients and the standard deviation ratio of the MME for the asymmetric part are all lower than the MME skill of the total SAM field (Figure 1). Meanwhile, the highest correlation coefficient is in SON, and the lowest correlation coefficient is in MAM for both the AMIP and historical experiments. Specifically, the centres of the SAM asymmetric part can basically be reproduced in DJF (Figure 7e,i), but the positions of these centres are at lower latitudes than ERA-Interim (Figure 7a). In MAM, only the asymmetric part

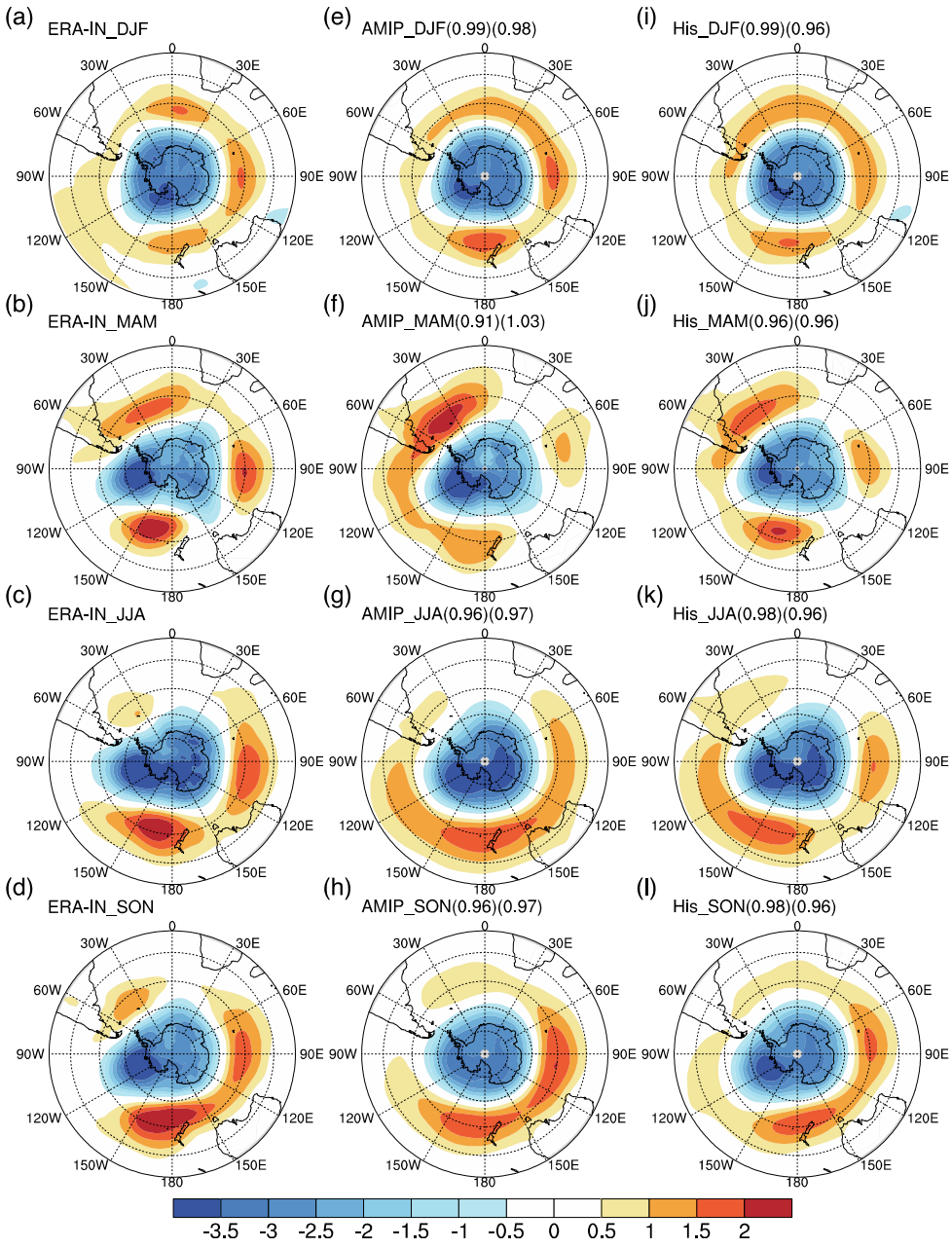

FIGURE 6 The SAM pattern in the four seasons after the best ensemble average. From left to right, the number in the first bracket indicates the correlation coefficient, and the number in the second bracket indicates the standard deviation ratio [Colour figure can be viewed at wileyonlinelibrary.com]

in the Western Hemisphere can be reproduced (Figure 7f,j), while the asymmetric part in the Eastern Hemisphere is missing. Additionally, although the standard deviation ratios are both underestimated in the AMIP and historical experiments, the overall skills in the AMIP experiment are higher than those in the historical experiment for all seasons.

To understand the sensitivity of ensemble members on the asymmetric part of the SAM simulation, we show box plots of the pattern correlation coefficient and standard deviation ratio of the asymmetric part for each model in Figures 8 and 9, respectively. It is clear that the model skills of the correlation coefficients have a large degree of dispersion for all seasons (Figure 8). Compared to the simulation skill of the total field (Figure 3), the model spread in MAM is similar, while in other seasons, the model spreads are relatively small. This result indicates that the simulation of the asymmetric part plays an important role in the spatial pattern simulation of the SAM in MAM, partly because the asymmetric structure is strong and complicated in this season.

The standard deviation ratio for the asymmetric part of the SAM is shown in Figure 9. In DJF (Figure 9a), the standard deviation ratio varies from 0.76 to 2.71. For most ensemble members of the model, the standard deviation ratio is greater than 1, and the amplitude of the asymmetric part simulation is stronger than the amplitude of the asymmetric part in the ERA-Interim. This

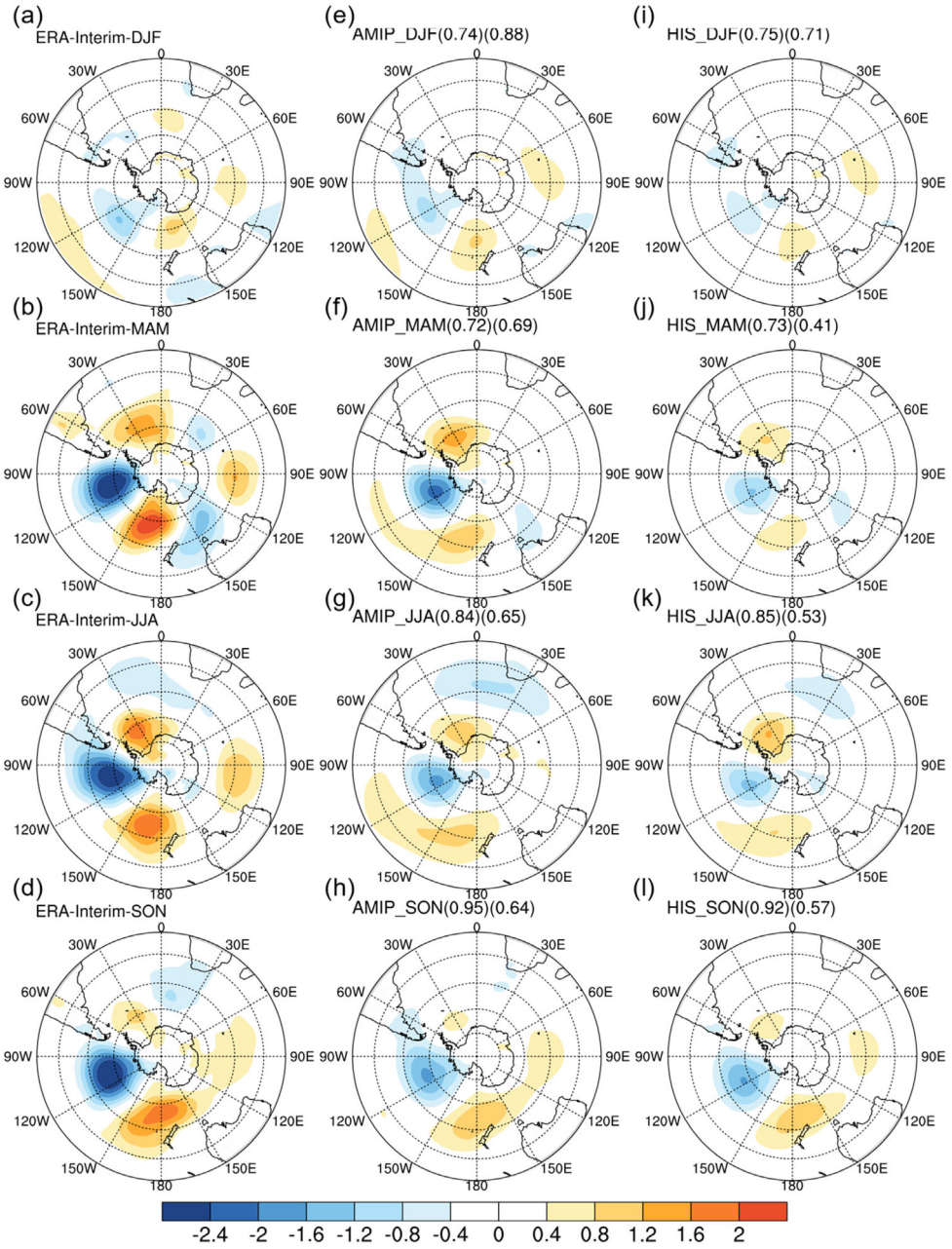

FIGURE 7 The asymmetric part of the SAM for the four seasons in ERA-Interim (a–d) and MME (e–l). From left to right (e–l), the number in the first bracket indicates the correlation coefficient, and the number in the second bracket indicates the standard deviation ratio [Colour figure can be viewed at wileyonlinelibrary.com]

finding may be the reason why the simulation of the SAM amplitude is relatively strong in DJF (Figure 4a). In MAM (Figure 9b), the standard deviation ratio varies from 0.32–1.58. In JJA (Figure 9c), the standard deviation ratio varies from 0.50 to 1.83. For the simulations of the asymmetric parts in MAM and JJA, some model ensemble members are relatively strong (relative to ERA-Interim), and some model ensemble members are relatively weak (relative to ERA-Interim) (Figure 9b,c). In SON (Figure 9d), the standard deviation ratio varies from 0.43 to 1.50. For this season, the simulated amplitudes of most model ensemble members are weak. Except in DJF, the correlation between the amplitude simulation of the asymmetric part and the SAM amplitude simulation in the other three seasons needs further study. In MAM (Figure 9b), most of the ensemble simulations in the AMIP experiment seem to have larger amplitudes than in the historical experiment. In other seasons (Figure 9a,c, d), the two experiments do not show much difference in the simulation of the amplitude (asymmetric part of the SAM).

The above analysis indicates that the simulation of the asymmetric part of the SAM is important to the simulation of the SAM total field, especially in MAM. Thus, the skill of the asymmetric part simulation may be highly correlated with the simulation of the total SAM. To quantify the relationship between the asymmetric part of the SAM and the SAM spatial pattern, the linear regression

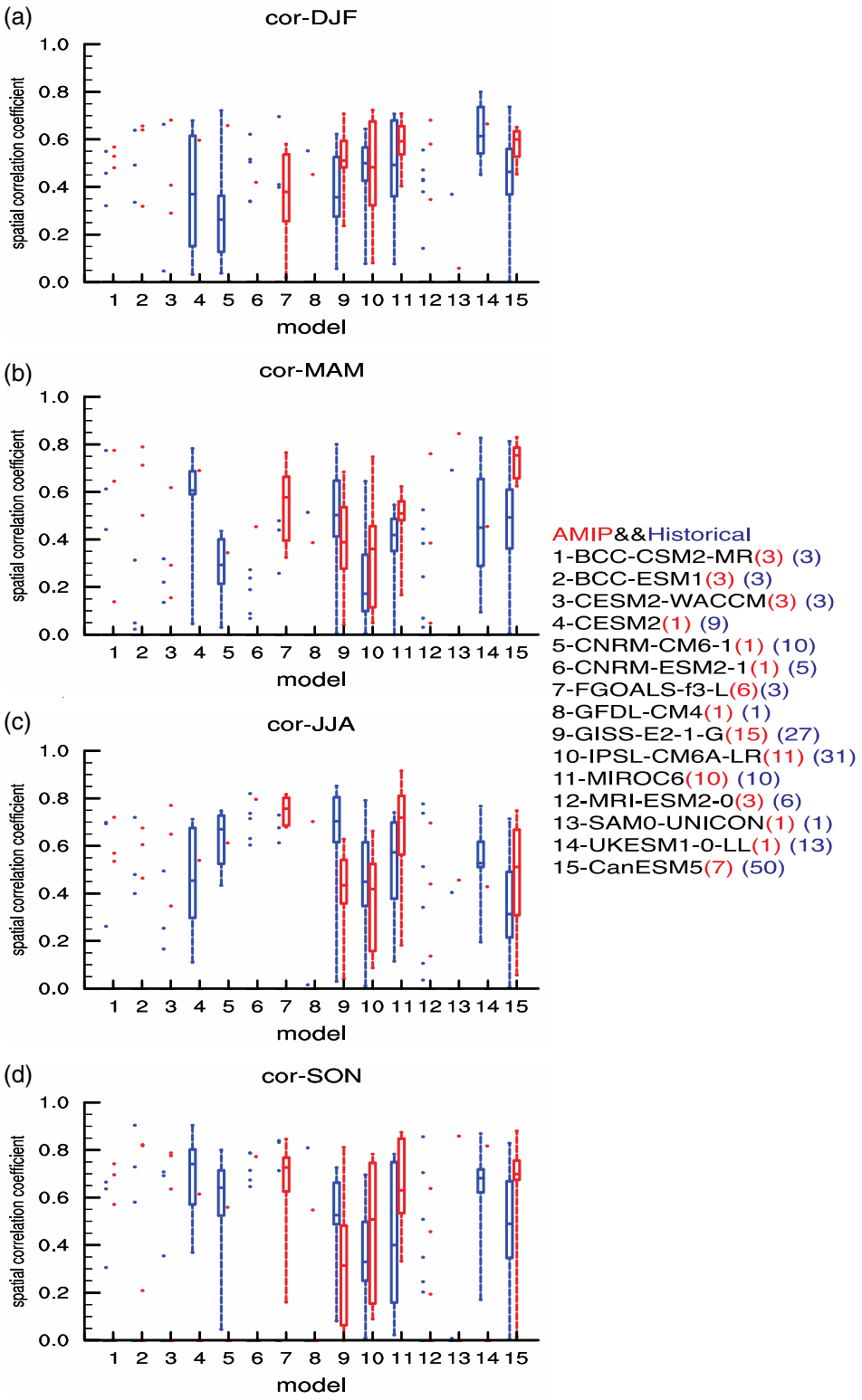

FIGURE 8 Correlation coefficients of the asymmetric part of the SAM for the four season simulations in the AMIP and historical experiments. The *X*-axis represents all models, and the *Y*-axis represents the spatial correlation coefficient. The red number indicates the number of ensembles in the model for the AMIP experiment, and the blue number indicates the number of ensembles in the model for the historical experiment [Colour figure can be viewed at wileyonlinelibrary.com]

between the two (the correlation coefficient of the asymmetric part and the correlation coefficient of the SAM pattern) is calculated for four seasons in Figure 10. This shows that the simulation of the SAM asymmetry has a good relationship with the spatial pattern simulation. The regression coefficients in the AMIP experiment are 0.03 in DJF, 0.11 in MAM, 0.11 in JJA, and 0.11 in SON, while in the historical experiment, the regression coefficients are 0.04 in DJF, 0.12 in MAM, 0.14 in JJA, and 0.09 in SON.

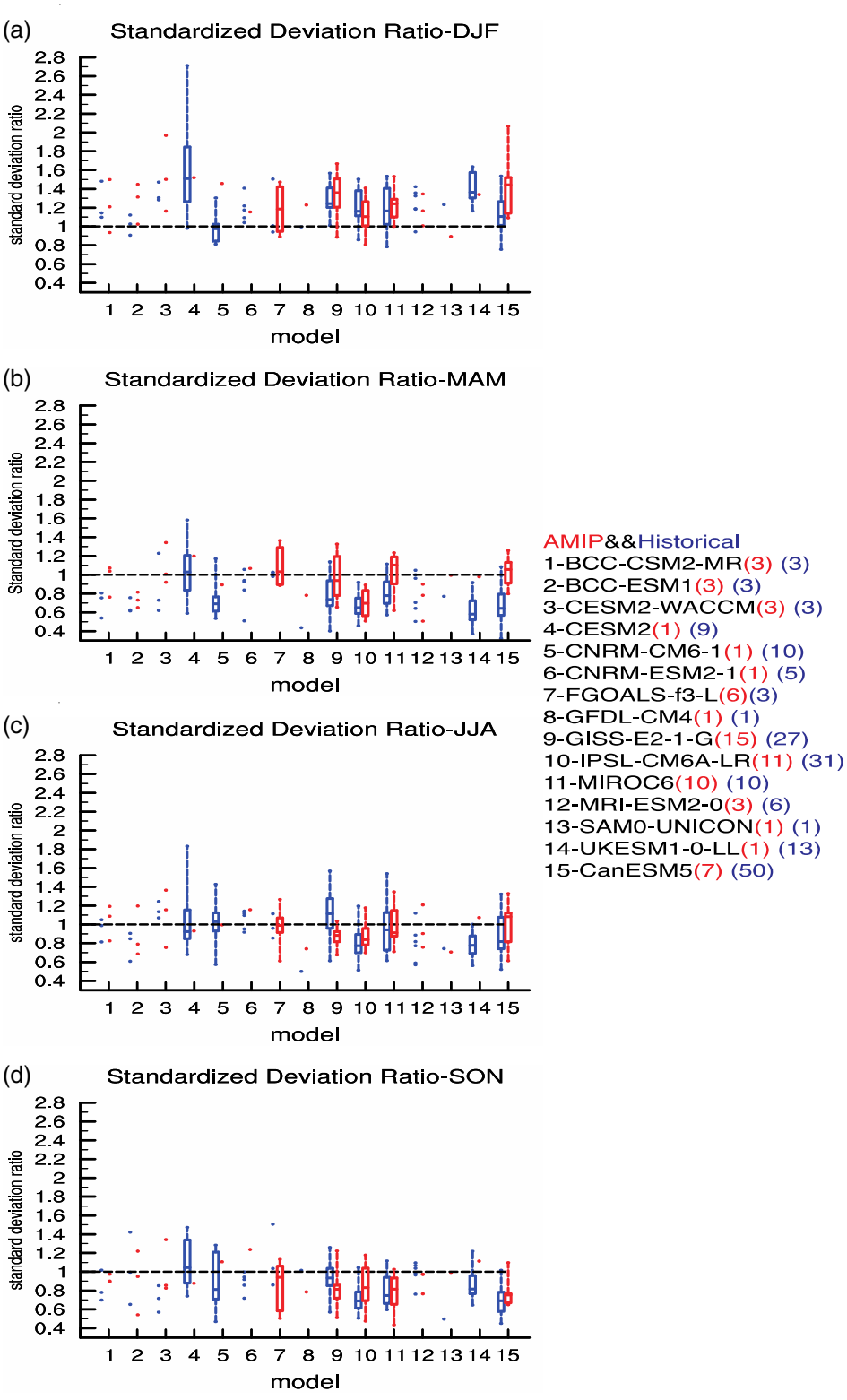

FIGURE 9 Standard deviation ratios of the asymmetric part of the SAM for the four season simulations in the AMIP and historical experiments. The *X*-axis represents all models, and the *Y*-axis represents the standard deviation ratio. The red number indicates the number of ensembles in the model for the AMIP experiment, and the blue number indicates the number of ensembles in the model for the historical experiment [Colour figure can be viewed at wileyonlinelibrary.com]

The above results indicate that the quality of the SAM asymmetric part of the simulation substantially affects the SAM simulation, whether it is an AMIP experiment or a historical experiment. It is important to note that in DJF, the correlation coefficient of the SAM pattern is generally good, but the correlation coefficient of the asymmetric part simulation is low, which suggests that the contribution of the asymmetric part to the total SAM is weak in DJF. By comparing MAM with the other three seasons, the points in MAM are more scattered, which

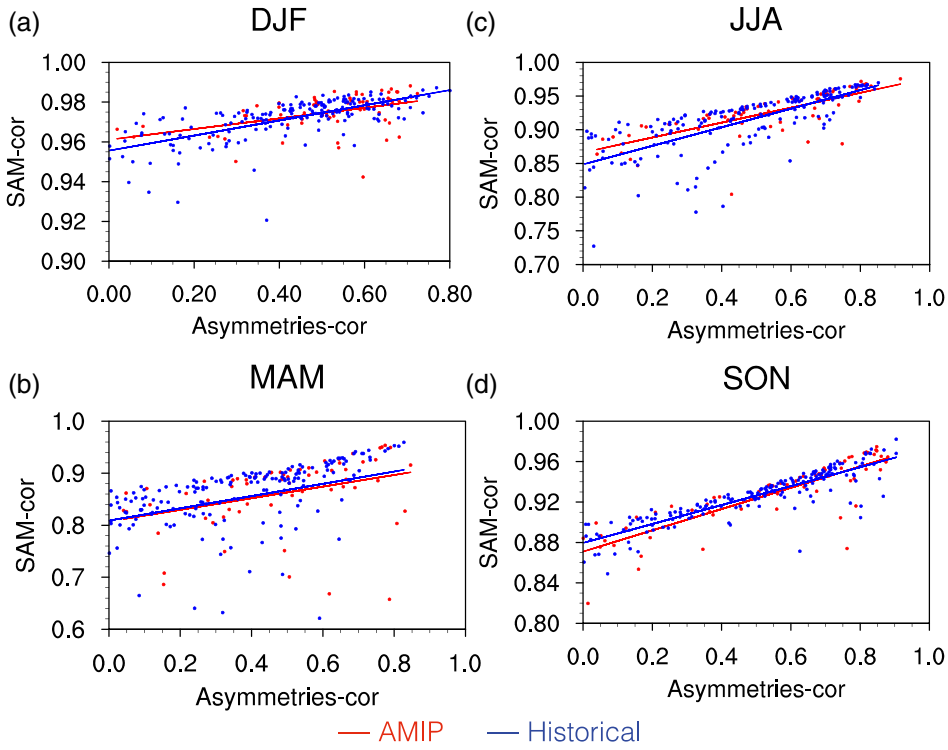

FIGURE 10 Scatterplot of four seasonal correlation coefficients in the AMIP experiment and the historical experiment. The *X*-axis represents the correlation coefficient of the asymmetric part (ensemble members and ERA-Interim) in Figure 8. The *Y*-axis represents the correlation coefficient of the SAM pattern (ensemble members and ERA-Interim) in Figure 3. The black lines represent the linear trends. The red dots and lines represent the AMIP experiment, and the blue dots and lines represent the historical experiment. (a) DJF, (b) MAM, (c) JJA, and (d) SON [Colour figure can be viewed at wileyonlinelibrary.com]

implies that the asymmetric part is not the only influence on the SAM simulation, and the symmetric part is also important.

4 | CONCLUSIONS AND DISCUSSION

In this study, the simulation skill of the seasonal spatial patterns of SAM in the AMIP and historical experiments from CMIP6 multimodels were evaluated. EOF analysis was performed for the PSL anomalies from the ERA-Interim and model data to extract SAM, which is the principal mode of variability of atmospheric circulation in the SH extratropical region.

In ERA-Interim, the SAM spatial pattern presents the opposite signs between the middle and high latitudes with a zonal three-wave structure in the middle latitudes (positive phase). The MME could basically capture the spatial patterns of the SAM for four seasons in the two experiments. However, the skill of MME varies from different seasons. The skill in DJF is the highest, while skill in MAM is lowest. For MME amplitude simulation of the SAM, most of the models overestimate the SAM amplitude, especially in DJF for both AMIP and historical simulations.

In general, the calculated SAM pattern is found to be sensitive to the number of ensemble members. However, the SAM amplitude simulation is not very sensitive to the number of ensemble members. Additionally, the degree of sensitivity of the SAM to the number of ensemble members is model-dependent. For the comparisons between AMIP and historical experiments, the AMIP simulation skill in capturing the SAM pattern is overall comparable with historical simulation, but the SAM amplitude simulation is sensitive to ensemble members when air–sea interaction is involved. Furthermore, the interaction between the atmosphere and the ocean may play an important role in the SAM simulation in reducing the amplitude simulation biases. SST variability may affect the SAM pattern, which is consistent with the research of Ding *et al.* (2012).

The asymmetric part of SAM is very important for the total field. The MME could capture the spatial pattern, especially the positive and negative centres in the Western Hemisphere. However, the pattern in the Eastern Hemisphere, especially in MAM, cannot be captured. Furthermore, the amplitude of the SAM asymmetric part is severely underestimated in MME. The simulations of the SAM asymmetric part are found to be sensitive to the simulation skill of the SAM spatial pattern, especially in MAM. Although the skill in DJF is high, the skill of the asymmetric part in DJF is relatively low. This result means that in the observation, the contribution of the asymmetric SAM part to the total field is small in DJF. Thus, we advocate that the evaluation of SAM needs to be focused on the MAM season to clearly understand the model biases

arising from the asymmetric part and to improve the model in the future.

Finally, a linear relationship of the correlation coefficient between the asymmetric part and the total SAM is also studied. The result indicates that the simulation of the SAM asymmetric part is crucial for the simulation of the SAM total field. From the perspective of atmospheric dynamics, the simulation of the SAM asymmetric part is dynamically related to heating due to latent heat in the Tropics. Condensation heating could produce Rossby waves and propagate along the westerly belt, affecting the mid-high latitude structure of the SAM (He and Yang, 2018). The location of latent heating over the tropical ocean can affect stationary wave anomalies in the upper troposphere (Lau, 1992). Thus, whether it can correctly simulate the location of the latent heat heating of the tropical zone may be the key to affecting the asymmetric part of the SAM and the key to the SAM simulation. From this perspective, we will explore the relationship between the SAM and tropical precipitation in future studies to understand the formation and variation in the SAM.

ACKNOWLEDGEMENTS

The research presented in this paper was jointly funded by the Strategic Priority Research Program of the Chinese Academy of Sciences (grant no. XDA19070404), the National Natural Science Foundation of China (grant no. 42030602), and the National Key Research and Development Program of China (grant nos. 2020YFA0608903 and 2017YFA0604004).

AUTHOR CONTRIBUTIONS

Xiaoqi Zhang: Formal analysis; writing – original draft. **Bian He:** Supervision; writing – review and editing. **Qing Bao:** Software. **Fei Zheng:** Writing – review and editing. **Jinxiao Li:** Software. **Wenting Hu:** Writing – review and editing. **Guoxiong Wu:** Writing – review and editing.

ORCID

Xiaoqi Zhang https://orcid.org/0000-0001-9999-0849
Fei Zheng https://orcid.org/0000-0001-6135-6148
Wenting Hu https://orcid.org/0000-0003-1770-4680

REFERENCES

Baldwin, M.P. and Thompson, D.W. (2009) A critical comparison of stratosphere–troposphere coupling indices. *Quarterly Journal of the Royal Meteorological Society*, 135, 1661–1672.

Boucher, O., Servonnat, J., Albright, A.L., Aumont, O., Balkanski, Y., Bastrikov, V., Bekki, S., Bonnet, R., Bony, S., Bopp, L., Braconnot, P., Brockmann, P., Cadule, P., Caubel, A., Cheruy, F., Codron, F., Cozic, A., Cugnet, D., D'Andrea, F., Davini, P., Lavergne, C., Denvil, S., Deshayes, J., Devilliers, M., Ducharne, A., Dufresne, J.L., Dupont, E., Éthé, C., Fairhead, L., Falletti, L., Flavoni, S., F., M.A., Gardoll, S., Gastineau, G., Ghattas, J., Grandpeix, J.Y., Guenet, B., Guez, L.E., Guilyardi, E., Guimberteau, M., Hauglustaine, D., Hourdin, F., Idelkadi, A., Joussaume, S., Kageyama, M., K., Myriam, K., Gerhard, L., N., Levavasseur, G., Lévy, C., Li, L., Lott, F., Lurton, T., Luyssaert, S., Madec, G., Madeleine, J.B., Maignan, F., Marchand, M., Marti, O., Mellul, L., Meurdesoif, Y., Mignot, J., Musat, I., O., C., Peylin, P., Planton, Y., Polcher, J., Rio, C., Rochetin, N., Rousset, C., Sepulchre, P., Sima, A., Swingedouw, D., Thiéblemont, R., Traore, Abdoul K., Vancoppenolle, M., Vial, J., Vialard, J., Viovy, N. and Vuichard, N. (2020) Presentation and evaluation of the IPSL-CM6A-LR climate model. *Journal of Advances in Modeling Earth Systems*, 12(7). https://doi.org/10.1029/2019ms002010

Codron, F. (2007) Relations between annular modes and the mean state: Southern Hemisphere winter. *Journal of the Atmospheric Sciences*, 64, 3328–3339.

Danabasoglu, G., Lamarque, J.-F., Bacmeister, J., Bailey, D. A., DuVivier, A. K., Edwards, J., Emmons, L. K., Fasullo, J., Garcia, R., Gettelman, A., Hannay, C., Holland, M. M., Large, W. G., Lauritzen, P. H., Lawrence, D. M., Lenaerts, J. T. M., Lindsay, K., Lipscomb, W. H., Mills, M. J., Neale, R., Oleson, K. W., Otto-Bliesner, B., Phillips, A. S., Sacks, W., Tilmes, S., Kampenhout, L., Vertenstein, M., Bertini, A., Dennis, J., Deser, C., Fischer, C., Fox-Kemper, B., Kay, J. E., Kinnison, D., Kushner, P. J., Larson, V. E., Long, M. C., Mickelson, S., Moore, J. K., Nienhouse, E., Polvani, L., Rasch, P. J. and Strand, W. G. (2020) The community earth system model version 2 (CESM2). *Journal of Advances in Modeling Earth Systems*, 12(2). https://doi.org/10.1029/2019ms001916

Dee, D.P., Uppala, S.M., Simmons, A.J., Berrisford, P., Poli, P., Kobayashi, S., Andrae, U., Balmaseda, M.A., Balsamo, G., Bauer, P., Bechtold, P., Beljaars, A.C.M., van de Berg, L., Bidlot, J., Bormann, N., Delsol, C., Dragani, R., Fuentes, M., Geer, A.J., Haimberger, L., Healy, S.B., Hersbach, H., Hólm, E. V., Isaksen, L., Kållberg, P., Köhler, M., Matricardi, M., McNally, A.P., Monge-Sanz, B.M., Morcrette, J.J., Park, B.K., Peubey, C., de Rosnay, P., Tavolato, C., Thépaut, J.N. and Vitart, F. (2011) The ERA-Interim reanalysis: configuration and performance of the data assimilation system. *Quarterly Journal of the Royal Meteorological Society*, 137, 553–597.

Ding, Q., Steig, E.J., Battisti, D.S. and Wallace, J.M. (2012) Influence of the Tropics on the southern annular mode. *Journal of Climate*, 25(18), 6330–6348.

Dou, J., Wu, Z. and Zhou, Y. (2017) Potential impact of the May Southern Hemisphere annular mode on the Indian summer monsoon rainfall. *Climate Dynamics*, 49, 1257–1269.

Dunne, J. P., Bociu, I., Bronselaer, B., Guo, H., John, J. G., Krasting, J. P., Stock, C. A., Winton, M. and Zadeh, N. (2020) Simple global ocean biogeochemistry with light, iron, nutrients and gas Version 2 (BLINGv2): Model description and simulation characteristics in GFDL's CM4.0. *Journal of Advances in Modeling Earth Systems*, 12(10), https://doi.org/10.1029/2019ms002008

Eyring, V., Bony, S., Meehl, G.A., Senior, C.A., Stevens, B., Stouffer, R.J. and Taylor, K.E. (2016) Overview of the coupled

model intercomparison project phase 6 (CMIP6) experimental design and organization. *Geoscientific Model Development*, 9, 1937–1958.

Ferreira, D., Marshall, J., Bitz, C.M., Solomon, S. and Plumb, A. (2015) Antarctic Ocean and sea ice response to ozone depletion: a two-time-scale problem. *Journal of Climate*, 28, 1206–1226.

Fogt, R.L., Jones, J.M. and Renwick, J. (2012) Seasonal zonal asymmetries in the Southern Annular Mode and their impact on regional temperature anomalies. *Journal of Climate*, 25, 6253–6270.

Fogt, R.L., Perlwitz, J., Monaghan, A.J., Bromwich, D.H., Jones, J. M. and Marshall, G.J. (2009) Historical SAM variability. Part II: twentieth-century variability and trends from reconstructions, observations, and the IPCC AR4 models. *Journal of Climate*, 22, 5346–5365.

Gates, W.L., Boyle, J.S., Covey, C., Dease, C.G., Doutriaux, C.M., Drach, R.S., Fiorino, M., Gleckler, P.J., Hnilo, J.J., Marlais, S.M., Phillips, T.J., Potter, G.L., Santer, B.D., Sperber, K.R., Taylor, K. E. and Williams, D.N. (1999) An overview of the results of the Atmospheric Model Intercomparison project (AMIP I). *Bulletin of the American Meteorological Society*, 80, 29–56.

Gettelman, A., Hannay, C., Bacmeister, J. T., Neale, R. B., Pendergrass, A. G., Danabasoglu, G., Lamarque, J.-F., Fasullo, J. T., Bailey, D. A., Lawrence, D. M. and Mills, M. J. (2019) High climate sensitivity in the community earth system model version 2 (CESM2). *Geophysical Research Letters*, 46(14), 8329–8337. https://doi.org/10.1029/2019gl083978

Gille, S.T. (2008) Decadal-scale temperature trends in the Southern Hemisphere Ocean. *Journal of Climate*, 21, 4749–4765.

Gillett, N. and Fyfe, J. (2013) Annular mode changes in the CMIP5 simulations. *Geophysical Research Letters*, 40, 1189–1193.

Gong, D. and Wang, S. (1998) Antarctic oscillation: concept and applications. *Chinese Science Bulletin*, 43, 734–738.

Gong, D. and Wang, S. (1999) Definition of antarctic oscillation index. *geophysical research letters*, 26(4), 459–462. https://doi.org/10.1029/1999gl900003

He, B., Bao, Q., Wang, X., Zhou, L., Wu, X., Liu, Y., Wu, G., Chen, K., He, S., Hu, W., Li, J., Li, J., Nian, G., Wang, L., Yang, J., Zhang, M. and Zhang, X. (2019) CAS FGOALS-f3-L model datasets for CMIP6 historical atmospheric model Intercomparison project simulation. *Advances in Atmospheric Sciences*, 36, 771–778.

He, B. and Yang, S. (2018) Role of latent heating over the tropical Western Pacific in surface temperature change over North America during boreal spring. *Journal of Climate*, 31, 2169–2184.

Hendon, H.H., Thompson, D.W. and Wheeler, M.C. (2007) Australian rainfall and surface temperature variations associated with the Southern Hemisphere annular mode. *Journal of Climate*, 20, 2452–2467.

Ho, M., Kiem, A.S. and Verdon-Kidd, D.C. (2012) The southern annular mode: a comparison of indices. *Hydrology and Earth System Sciences*, 16, 967–982.

Ito, G., Romanou, A., Kiang, N.Y., Faluvegi, G., Aleinov, I., Ruedy, R., Russell, G., Lerner, P., Kelley, M. and Lo, K. (2020) Global carbon cycle and climate feedbacks in the NASA GISS ModelE2.1. *Journal of Advances in Modeling Earth Systems*, 12(10). https://doi.org/10.1029/2019ms002030

Kidson, J.W. and Sinclair, M.R. (1995) The influence of persistent anomalies on Southern Hemisphere storm tracks. *Journal of Climate*, 8, 1938–1950.

Kidston, J., Renwick, J. and McGregor, J. (2009) Hemispheric-scale seasonality of the Southern Annular Mode and impacts on the climate of New Zealand. *Journal of Climate*, 22, 4759–4770.

Kwok, R. and Comiso, J.C. (2002) Spatial patterns of variability in Antarctic surface temperature: connections to the Southern Hemisphere Annular Mode and the Southern Oscillation. *Geophysical Research Letters*, 29, 1–4.

Lau, K.-M. (1992) East Asian summer monsoon rainfall variability and climate teleconnection. *Journal of the Meteorological Society of Japan*, 70, 211–242.

Lee, D.Y., Petersen, M.R. and Lin, W. (2019) The southern annular mode and southern ocean surface westerly winds in E3SM. *Earth and Space Science*, 6, 2624–2643.

Lefebvre, W., Goosse, H., Timmermann, R. & Fichefet, T. (2004) Influence of the Southern Annular Mode on the sea ice–ocean system. *Journal of Geophysical Research*, 109(C9), https://doi.org/10.1029/2004jc002403

Limpasuvan, V. and Hartmann, D.L. (1999) Eddies and the annular modes of climate variability. *Geophysical Research Letters*, 26, 3133–3136.

Liu, T., Li, J., Li, Y.J., Zhao, S., Zheng, F., Zheng, J. and Yao, Z. (2018) Influence of the may southern annular mode on the south china sea summer monsoon. *Climate Dynamics*, 51, 4095–4107.

Lu, R., Li, Y. and Buwen, D. (2007) Arctic oscillation and Antarctic oscillation in internal atmospheric variability with an ensemble AGCM simulation. *Advances in Atmospheric Sciences*, 24, 152–162.

Mo, K.C. (2000) Relationships between low-frequency variability in the Southern Hemisphere and sea surface temperature anomalies. *Journal of Climate*, 13, 3599–3610.

Morgenstern, O. (2021) The southern annular mode in 6th coupled model intercomparison project models. *Journal of Geophysical Research*, 126(5), e2020JD034161.

Nan, S., Li, J., Yuan, X. and Zhao, P. (2009) Boreal spring Southern Hemisphere Annular Mode, Indian Ocean sea surface temperature, and East Asian summer monsoon. *Journal of Geophysical Research*, 114(D2). https://doi.org/10.1029/2008jd010045

Nan, S. and Li, J. (2003) The relationship between the summer precipitation in the Yangtze River valley and the boreal spring Southern Hemisphere annular mode. *Geophysical Research Letters*, 30(24), https://doi.org/10.1029/2003gl018381

Nan, S., Yang, J., Bao, Y., Li, J. and Rong, X. (2019) Simulation of the Northern and Southern Hemisphere annular modes by CAMS-CSM. *Journal of Meteorological Research*, 33, 934–948.

Park, S., Shin, J., Kim, S., Oh, E. and Kim, Y. (2019) Global climate simulated by the seoul national university atmosphere model version 0 with a unified convection scheme (SAM0-UNICON). *Journal of Climate*, 32(10), 2917–2949. https://doi.org/10.1175/jcli-d-18-0796.1

Qian, Z., Wang, H. and Sun, J.J.A.M.S. (2011) The hindcast of winter and spring Arctic and Antarctic Oscillation with the coupled climate models, 25, 340–354.

Séférian, R., Nabat, P., Michou, M., Saint-Martin, D., Voldoire, A., Colin, J., Decharme, B., Delire, C., Berthet, S., Chevallier, M., Sénési, S., Franchisteguy, L., Vial, J., Mallet, M., Joetzjer, E., Geoffroy, O., Guérémy, J.F., Moine, M.P., Msadek, R., Ribes, A., Rocher, M., Roehrig, R., Salas-y-Mélia, D., Sanchez, E., Terray, L., Valcke, S., Waldman, R., Aumont, O.,

Bopp, L., Deshayes, J., Éthé, C. and Madec, G. (2019) Evaluation of CNRM Earth System Model, CNRM-ESM2-1: Role of Earth System Processes in Present-Day and Future Climate. *Journal of Advances in Modeling Earth Systems*, 11(12), 4182–4227. https://doi.org/10.1029/2019ms001791

Spence, P., Griffies, S.M., England, M.H., Hogg, A.M.C., Saenko, O. A. and Jourdain, N.C. (2014) Rapid subsurface warming and circulation changes of Antarctic coastal waters by poleward shifting winds: antarctic subsurface ocean warming. *Geophysical Research Letters*, 41, 4601–4610.

Swart, N.C., Cole, J.N.S., Kharin, V.V., Lazare, M., Scinocca, J.F., Gillett, N.P., Anstey, J., Arora, V., Christian, J.R., Hanna, S., Jiao, Y., Lee, W.G., Majaess, F., Saenko, O.A., Seiler, C., Seinen, C., Shao, A., Sigmond, M., Solheim, L., von Salzen, K., Yang, D. and Winter, B. (2019) The Canadian Earth System Model version 5 (CanESM5.0.3). *Geoscientific Model Development*, 12(11), 4823–4873. https://doi.org/10.5194/gmd-12-4823-2019

Sellar, A.A., Jones, C.G., Mulcahy, J.P., Tang, Y., Yool, A., Wiltshire, A., O'Connor, F.M., Stringer, M., Hill, R., Palmieri, J., Woodward, S., Mora, L., Kuhlbrodt, T., Rumbold, S.T., Kelley, D. I., Ellis, R., Johnson, C.E., Walton, J., Abraham, N.L., Andrews, M.B., Andrews, T., Archibald, A.T., Berthou, S., Burke, E., Blockley, E., Carslaw, K., Dalvi, M., Edwards, J., Folberth, G.A., Gedney, N., Griffiths, P.T., Harper, A.B., Hendry, M.A., Hewitt, A.J., Johnson, B., Jones, A., Jones, C.D., Keeble, J., Liddicoat, S., Morgenstern, O., Parker, R.J., Predoi, V., Robertson, E., Siahaan, A., Smith, R.S., Swaminathan, R., Woodhouse, M.T., Zeng, G. and Zerroukat, M. (2019) UKESM1: description and evaluation of the U.K. earth system model. *Journal of Advances in Modeling Earth Systems*, 11(12), 4513–4558. https://doi.org/10.1029/2019ms001739

Tatebe, H., Ogura, T., Nitta, T., Komuro, Y., Ogochi, K., Takemura, T., Sudo, K., Sekiguchi, Miho, Abe, M., Saito, F., Chikira, M., Watanabe, S., Mori, M., Hirota, N., Kawatani, Y., Mochizuki, T., Yoshimura, K., Takata, K., O'ishi, R., Yamazaki, Dai, Suzuki, T., Kurogi, M., Kataoka, T., Watanabe, M. and Kimoto, M. (2019) Description and basic evaluation of simulated mean state, internal variability, and climate sensitivity in MIROC6. *Geoscientific Model Development*, 12(7), 2727–2765. https://doi.org/10.5194/gmd-12-2727-2019

Taylor, K.E. (2001) Summarizing multiple aspects of model performance in a single diagram. *Journal of Geophysical Research: Atmospheres*, 106, 7183–7192.

Taylor, K.E. (2005). Taylor diagram primer. Working paper 1-4.

Thompson, D.W. and Solomon, S. (2002) Interpretation of recent Southern Hemisphere climate change. *Science*, 296, 895–899.

Thompson, D.W.J. and Wallace, J.M. (2000) Annular modes in the extratropical circulation. Part I: month-to-month variability. *Journal of Climate*, 13, 1000–1016.

Thompson, D.W.J., Wallace, J.M. and Hegerl, G.C. (2000) Annular modes in the extratropical circulation. Part II: Trends. *Journal of Climate*, 13, 1018–1036.

Voldoire, A., Saint-Martin, D., Sénési, S., Decharme, B., Alias, A., Chevallier, M., Colin, J., Guérémy, J.-F., Michou, M., Moine, M.-P., Nabat, P., Roehrig, R., Salas y Mélia, D., Séférian, R., Valcke, S., Beau, I., Belamari, S., Berthet, S., Cassou, C., Cattiaux, J., Deshayes, J., Douville, H., Ethé, C., Franchistéguy, L., Geoffroy, O., Lévy, C., Madec, G., Meurdesoif, Y., Msadek, R., Ribes, A., Sanchez-Gomez, E., Terray, L. and Waldman, R. (2019) Evaluation of CMIP6 DECK Experiments With CNRM-CM6-1. *Journal of Advances in Modeling Earth Systems*, 11(7), 2177–2213. https://doi.org/10.1029/2019ms001683

Wu, Z., Dou, J. and Lin, H. (2015) Potential influence of the November–December Southern Hemisphere annular mode on the East Asian winter precipitation: a new mechanism. *Climate Dynamics*, 44, 1215–1226.

Wu, Z., Li, J., Wang, B. and Liu, X. (2009) Can the Southern Hemisphere annular mode affect China winter monsoon?. *Journal of Geophysical Research*, 114(D11), https://doi.org/10.1029/2008jd011501

Wu, T., Lu, Y., Fang, Y., Xin, X., Li, L., Li, W., Jie, W., Zhang, J., Liu, Y., Zhang, L., Zhang, F., Zhang, Y., Wu, F., Li, J., Chu, M., Wang, Z., Shi, X., Liu, X., Wei, M., Huang, A., Zhang, Y. and Liu, X. (2019) The Beijing Climate Center Climate System Model (BCC-CSM): the main progress from CMIP5 to CMIP6. *Geoscientific Model Development*, 12(4), 1573–1600. https://doi.org/10.5194/gmd-12-1573-2019

Wu, T., Zhang, F., Zhang, J., Jie, W., Zhang, Y., Wu, F., Li, L., Yan, J., Liu, X., Lu, X., Tan, H., Zhang, L., Wang, J. and Hu, A. (2020) Beijing climate center earth system model version 1 (BCC-ESM1): model description and evaluation of aerosol simulations. *Geoscientific Model Development*, 13(3), 977–1005. https://doi.org/10.5194/gmd-13-977-2020

Yali, Z. and Huijun, W. (2010) The arctic and antarctic oscillations in the IPCC AR4 coupled models. *Journal of Meteorological Research*, 24, 176–188.

Yukimoto, S., Kawai, H., Koshiro, T., Oshima, N., Yoshida, K., Urakawa, S., Tsujino, H., Deushi, M., Tanaka, T., Hosaka, M., Yabu, S., Yoshimura, Hiromasa, Shindo, E., Mizuta, R., Obata, A., Adachi, Y. and Ishii, M. (2019) The meteorological research institute earth system model version 2.0, MRI-ESM2.0: Description and basic evaluation of the physical component. *Journal of the Meteorological Society of Japan. Ser. II*, 97(5), 931–965. https://doi.org/10.2151/jmsj.2019-051

Zhao, N., Liang, S. and Ding, Y. (2012) Coupling modes among action centers of wave–mean flow interaction and their association with the AO/NAM. *Journal of Climate*, 25, 447–458.

Zheng, F., Li, J., Clark, R.T. and Nnamchi, H.C. (2013) Simulation and projection of the Southern Hemisphere annular mode in CMIP5 models. *Journal of Climate*, 26, 9860–9879.

Zheng, F., Li, J., Wang, L., Xie, F. and Li, X. (2015) Cross-seasonal influence of the December–February Southern Hemisphere annular mode on March–May Meridional circulation and precipitation. *Journal of Climate*, 28, 6859–6881.

SUPPORTING INFORMATION

Additional supporting information may be found in the online version of the article at the publisher's website.

How to cite this article: Zhang, X., He, B., Liu, Y., Bao, Q., Zheng, F., Li, J., Hu, W., & Wu, G. (2021). Evaluation of the seasonality and spatial aspects of the Southern Annular Mode in CMIP6 models. *International Journal of Climatology*, 1–18. https://doi.org/10.1002/joc.7447